

Lateral Charge Carrier Transport in Cu(In,Ga)Se₂ Studied by Time-Resolved Photoluminescence Mapping

Mario Ochoa,* Shiro Nishiwaki, Shih-Chi Yang, Ayodhya N. Tiwari, and Romain Carron*

Electronic transport in a semiconductor is key for the development of more efficient devices. In particular, the electronic transport parameters carrier lifetime and mobility are of paramount importance for the modeling, characterization, and development of new designs for solar cells and optoelectronic devices. Herein, time-resolved photoluminescence mapping under low injection and wide-field illumination conditions is used to measure the carrier lifetime and analyze the lateral charge carrier transport in Cu(In,Ga)Se₂ absorbers grown at different temperatures, on different substrates, and subject to different post-deposition treatments (PDT) with light or heavy alkalis. To estimate the carrier mobility, numerical simulations of carrier diffusion transport to areas of increased recombination (defects) are used, similarly as observed experimentally. Mobilities are found in the range of 10–50 cm² V⁻¹ s⁻¹, and effective minority carrier lifetime between 100 and 800 ns resulting in carrier diffusion lengths of 2–9 μm depending on the sample. Finally, the factors limiting carrier mobility and the implications of carrier diffusion on the measured carrier lifetimes are discussed.

1. Introduction

Recombination and transport properties such as charge carrier lifetime and mobility are key parameters determining the performance of a solar cell. The minority carrier lifetime affects directly, and primarily, the open-circuit voltage. The minority carrier mobility influences directly the collection of charge carriers upon illumination, which has a direct impact on the photocurrent generation. On the one hand, in state-of-the-art solar cells, the charge carrier collection efficiency is near-unity, thus mobilities and carrier lifetimes are sufficient for the collection of photogenerated carriers.^[1] On the other hand, the charge carrier mobility can also influence the open-circuit voltage of the

devices in two main scenarios: 1) high surface recombination cases, in which a high charge carrier mobility enhances the flow of carriers to regions of high interface recombination, and 2) low mobility cases, in which local recombination is promoted by the slow flow of charge carriers, which, in turn, hinders the charge extraction out of the device. Therefore, it is of paramount importance to know the charge carrier lifetime and mobility to evaluate the photovoltaic performance and limitations of solar cells, especially at the operating conditions, i.e., one-sun, and to provide empirical input parameters for modeling of current and next-generation Cu(In,Ga)Se₂ (CIGS) solar cells.

A large variety of measurement systems were used to characterize recombination and carrier transport properties such as carrier lifetime,^[2,3] mobility,^[4] diffusion length,^[5–8] and even access to diode parameters:^[9] cathodoluminescence,^[10] electroluminescence,^[11] steady-state photoluminescence (PL),^[12,13] time-resolved THz spectroscopy,^[4,14] time of flight (ToF),^[15] time-resolved microwave conductivity (TRMC), lock-in thermography,^[16] laser-beam-induced current (LBIC),^[16] electron-beam-induced current (EBIC),^[17,18] two-photon spectroscopy,^[19] and transport imaging (scanning electron microscopy [SEM] coupled to a microscope and camera).^[20] Usually, more than one technique is required to determine the charge carrier lifetime or mobility. However, it is often very challenging (or not possible) to perform such measurements under equivalent injection conditions, especially at one-sun nominal operating conditions.

Several studies regarding recombination lifetimes for CIGS solar cells are reported in the literature, with time-resolved photoluminescence (TRPL) as the most used technique. Despite the difficulty in interpretation (see, e.g., Maiberg et al.^[21]), minority carrier lifetimes determined by TRPL are gathering agreement as a good metric for material quality evaluation in state-of-the-art CIGS solar cells.^[22–25] Determination of minority carrier mobility is more complex for CIGS considering bandgap gradients and few related reports exist. For instance, Strothkämper et al. used THz spectroscopy to determine intragrain mobilities for stoichiometric and Cu-poor CIS,^[26] and reported an electron mobility of 1000 and 200 cm² V⁻¹ s⁻¹, respectively. Kuciauskas et al. combined spectroscopic and TRPL studies to estimate the carrier mobility in graded absorbers (22–230 cm² V⁻¹ s⁻¹).^[27,28] More recently, Weiss et al. used TRPL measurements and numerical

M. Ochoa, S. Nishiwaki, S.-C. Yang, A. N. Tiwari, R. Carron
Laboratory for Thin Films and Photovoltaics
Empa-Swiss Federal Laboratories for Materials Science and Technology
Ueberlandstrasse 129, Dübendorf CH-8600, Switzerland
E-mail: Mario.ochoa@empa.ch; romain.carron@empa.ch

 The ORCID identification number(s) for the author(s) of this article can be found under <https://doi.org/10.1002/pssr.202100313>.

© 2021 The Authors. physica status solidi (RRL) Rapid Research Letters published by Wiley-VCH GmbH. This is an open access article under the terms of the Creative Commons Attribution License, which permits use, distribution and reproduction in any medium, provided the original work is properly cited.

DOI: 10.1002/pssr.202100313

simulations on CIS graded absorbers varying front and back surface interfaces to determine bulk lifetime and estimate the charge carrier mobility ($32\text{--}45\text{ cm}^2\text{ V}^{-1}\text{ s}^{-1}$).^[29] Chang et al. performed ultrafast transient spectroscopy to determine electron mobility ($\approx 8\text{--}60\text{ cm}^2\text{ V}^{-1}\text{ s}^{-1}$) by considering explicitly the influence of the bandgap grading profile in CIGS absorbers.^[30] Given the diversity of approaches and absorbers studied, namely, different Ga composition, bandgap grading, growth temperature, postdeposition treatments, and so on, it is beneficial to expand the literature to gather consensus and facilitate the comparison between results.

Most works studied the flow of carriers primarily in the vertical direction of the absorber—and within the grains—whereas few reports exist quantifying the flow of carriers in the lateral direction of polycrystalline CIGS. Other approaches or imaging techniques have been used to characterize the lateral charge carrier transport in other semiconductors.^[5,20] Such systems may use a focused laser beam and detect the photon emission of diffused carriers out of the beam using a scanning detection stage or a dedicated camera. Our system lacks a scanning detection stage or dedicated camera; thus, we did not explore these approaches. The main challenge for any spatially resolved system intended to characterize CIGS is to achieve low injection conditions without compromising the signal-to-noise ratio required for the measurement.

In this work, we used TRPL mapping under wide-field illumination to achieve low injection conditions. In this configuration, it is possible to characterize recombination lifetimes and the transport properties of the material under identical conditions, which are comparable with the solar cell operation, i.e., one-sun. Similar to the approach used by Gfroerer et al.,^[31] we examine the lateral carrier transport to extended defects. This provides additional insights into the role of grains and grain boundaries on the mobility and charge carrier lifetime of state-of-the-art CIGS solar cells. The carrier lifetime is directly measured in the vicinity of the defect, and the diffusion of carriers is analyzed by comparison with numerical simulations. This combination provides insight into the mechanisms governing carrier transport and allows estimating the carrier mobility. We apply the methodology to study the carrier transport properties of CIGS absorbers at different growth temperatures, substrate, and alkali postdeposition treatments.

Herein, first evidence of carrier transport near extended defective region is shown for four different CIGS samples. Then, we discuss and compare the estimation of the carrier mobility from luminescence methods in wide-field illumination (either scanning or camera-based techniques). The TRPL mapping datasets are analyzed by extracting curves fitted consistently against simulations to constrain the carrier mobility. Finally, we discuss the results and possible mechanisms dominating the carrier mobility of CIGS of different fabrication processes.

2. Results

2.1. Experimental evidence of lateral carrier diffusion from TRPL mapping

To study the lateral diffusion of charge carriers, we focus on the temporal variation of the PL signal near extended defects found

in CIGS absorbers of different material quality. **Figure 1** shows the time-gated PL intensity maps and their corresponding profiles for the four samples analyzed in this study (see Section 5 for samples description). The time gates illustrate the carrier diffusion over time and correspond to time-integrated portions of the decay at initial, middle, and end time ranges covering the full decay (see top graphs in Figure 1). These time gates are different for each sample (see caption of Figure 1) due to distinct lifetime, and will not be used further in the analysis. Detailed analysis including additional time gates is given in Section 2.3. Hereinafter, we define the area away the defect as a defect-free area, which exhibits a relatively homogeneous PL signal as compared with the defect site, and is subject to relatively weaker non-radiative recombination. The defect is the dark central region, which apparently expands over time. For NaF (top row maps), more than one individual defect can be seen at any time gate. No interaction between them is detected; thus, our analysis will only focus on the central defect. Only one clear defect is observed for NaF + RbF (low temperature [LT]) on soda-lime glass (SLG), which also expands over time. The defect in sample NaF + RbF SLG (high temperature [HT]) is not detected at early times. After an initial delay, the central defect becomes evident and its apparent size increases more than the previously described samples. For steel, a defective region with intricate shape is discernible at early times. The interaction of these distinguishable defects is evident by comparing the initial and end time, for which the extended influence of each defect merges to form a single dark region.

To quantify the carrier transport to the defect, centered angle-averaged profiles for SLG samples are shown on the right part of Figure 1 for the initial, middle, and end time. Gaussian fits are overlaid. The full width at half maximum (FWHM) of these fits increases between early time and end time by 3.5, 6, and 10 μm for NaF, NaF + RbF (LT), and NaF + RbF (HT), respectively. For steel, a centered average line profile cannot be used. Instead, a single cutline (depicted in Figure 1 at the initial time map) results in a net increase of FWHM of 5 μm between initial and end time.

An important implication of the technique used here is highlighted by the steel sample. Whereas the individual contribution of different defects are resolved at the initial time, at the end time (or using time-integrated data) the defects appear merged. This is a consequence of carrier diffusion from defective-free areas to the defect under wide-field illumination, exemplifying the loss of optical resolution of the technique, as previously shown,^[32] consistently with other studies found in the literature for GaAs and epitaxial CdTe.^[19,31,33]

2.2. Model validation

Figure 1 shows the profile can be modeled by a Gaussian formula. It is straightforward to plot FWHM as a function of time, which is a direct indicator of carrier diffusion. The FWHM can be linked to physical quantities such as carrier diffusivity.^[5] Wolford et al. derived a diffusion model that used FWHM.^[5] However, this model cannot be directly applied to our data, as it assumes uniform material properties free from defective regions whereas our experiments were performed under wide-field illumination with a defective region. In the following, we

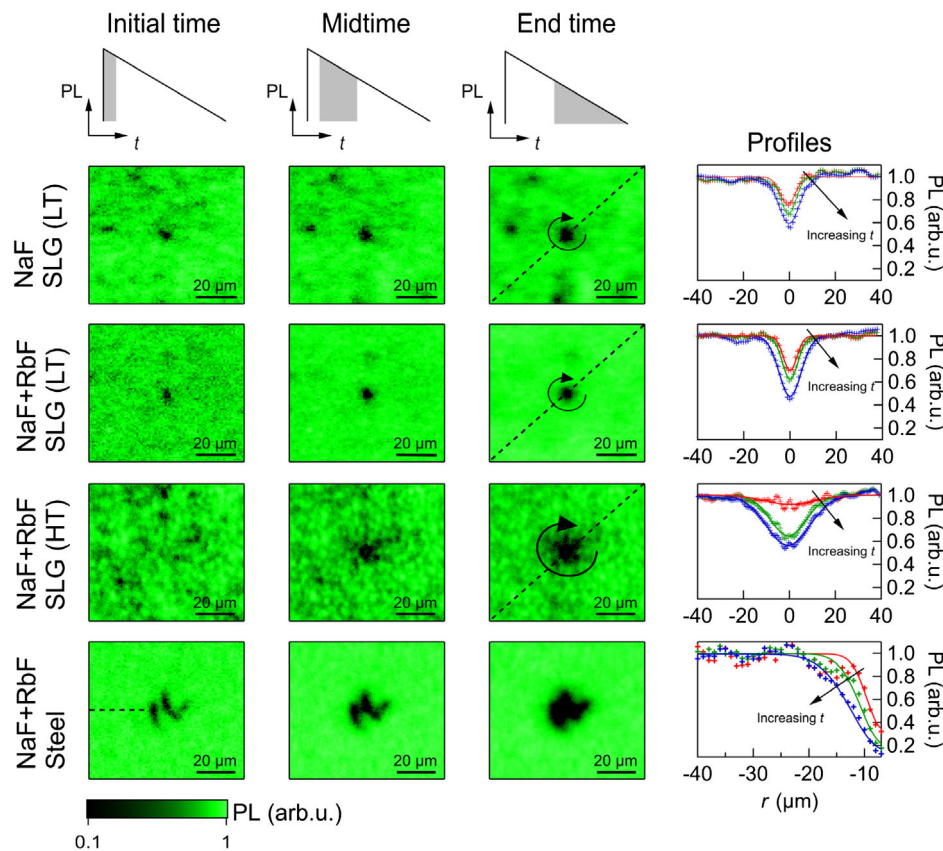


Figure 1. Top view normalized PL intensity maps of the four samples near defects integrated over different ranges of time delays, as shown by shaded regions of general TRPL illustration curves (top graphs). For NaF sample, the time ranges (in ns) are [0, 10], [10, 30], and [30, 300] for initial, middle, and end time, respectively. For NaF + RbF (LT): [0, 10], [10, 100], [100, 800]. For NaF + RbF (HT): [0, 150], [150, 500], [500, 2100]. For steel: [0, 10], [10, 70], [70, 700]. The averaged profiles (indicated in the images by the rotating arrows and horizontal dashed line for steel) of PL at different times are also depicted in the corresponding Gaussian fits (fourth column graphs).

show how these two situations differ, and how we can process our experimental data. We solve self-consistently the temporal continuity and transport equations by finite element method using Sentaurus tool from Synopsys. Although the technology computer aided-design (TCAD) modeling is less elegant than analytical solutions,^[34] it allows decoupling recombination at and near the defect from transport properties, as it will be shown later. It also provides further insight into charge carrier dynamics (see Figure S1, Supporting Information), and can be extended to include other physical models (e.g., fixed charge regions, grain boundary or interface recombination, and even realistic grain structures assigning specific properties to each grain and grain boundaries^[35]).

Two simulations have been conducted to investigate the influence of defects and illumination conditions on carrier diffusion, and to validate our model. First, a $200 \times 200 \mu\text{m}^2$ region was simulated with carriers generated only within a circular spot of $15 \mu\text{m}$ diameter with a step-like profile. These conditions reproduce the “PL spot broadening” experiments using a localized beam spot reported in, e.g., the study by Wolford et al.^[5] The effective carrier lifetime for this region is defined as τ_{top} .

Figure 2a shows the FWHM versus time with $\tau_{\text{top}} = 800$ ns and carrier mobility $\mu = 60 \text{ cm}^2 \text{ V}^{-1} \text{ s}^{-1}$. Carriers progressively

diffuse laterally from the illuminated to the nonilluminated area, as shown in Figure 2b,c. Wolford et al. derived an analytical expression to model the diffusive transport from a localized spot illumination: $\text{FWHM}^2(t) = 16 \ln(2)Dt + 4\ln(2)(\text{FWHM}_0)^2$, where FWHM_0 is the initial beam width and D is the diffusivity of the material. A very good agreement is obtained between the analytical solution (solid line) and TCAD calculations (empty circles). The simulations correctly capture the physics of carrier diffusion in the absorber layer.

In the second simulation, we define a centered defect (increased nonradiative recombination region) with the same diameter and generate carriers over the full area, to mimic our experimental wide-field illumination conditions. Instead of a well-defined illumination profile, we deal with uniform illumination and carrier recombination at the defect and subsequent carrier transport toward the defect. We introduce another parameter, $\tau_{\text{defect}} = 300$ ns. The curve labeled TCAD #1 (triangles) considers the same mobility ($60 \text{ cm}^2 \text{ V}^{-1} \text{ s}^{-1}$) and the same defect-free effective carrier lifetime ($\tau_{\text{top}} = 800$ ns), as the “PL spot broadening” case. The FWHM also increases with time; however, the increase is significantly less than the “PL spot broadening” case.

The higher FWHM sensitivity for the “PL spot broadening” approach originates from the large gradient of photogenerated

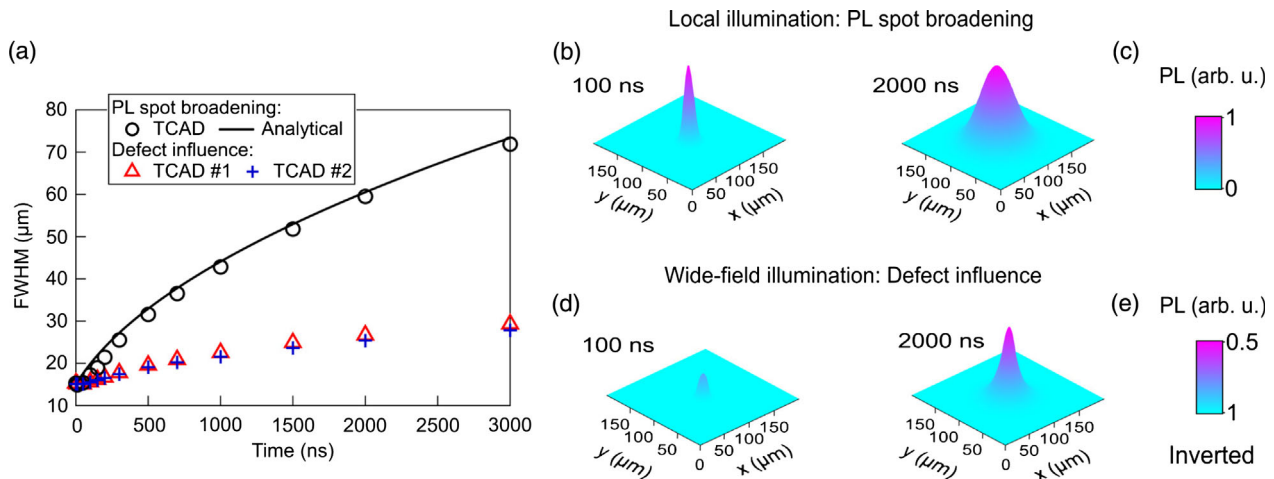


Figure 2. a) FWHM as a function of time calculated with an analytical diffusion model (solid line), TCAD simulations emulating the lateral diffusion of carriers after local excitation (empty circles), TCAD simulations assuming a central defect reproducing our experimental conditions (wide-field illumination), for two pairs of mobility and defect lifetime: 1) TCAD #1: $60 \text{ cm}^2 \text{ V}^{-1} \text{ s}^{-1}$ and 300 ns and 2) TCAD #2: $30 \text{ cm}^2 \text{ V}^{-1} \text{ s}^{-1}$ and 80 ns . b, c) The “PL spot broadening” case at 100 ns and 2000 ns , respectively. d, e) PL in the case of wide-field illumination in the presence of the defect at 100 ns and 2000 ns , respectively. Note that (d) and (e) use different and inverted z-value in the scale bar for better visualization.

carriers of several orders of magnitude between the illuminated and nonilluminated area (e.g., shown as PL in Figure 2b). On the contrary, the gradient between the defect and the defect-free area remains weak for the defect case, in which the full area is illuminated, as shown in Figure 2d.

As compared with the “PL spot broadening” method, modeling a defect adds a degree of freedom to the system: different combinations of mobility and defect lifetime values can produce similar FWHM(t) curves. Figure 2a shows the outcome of a second set of parameters: TCAD #2 (crosses, $30 \text{ cm}^2 \text{ V}^{-1} \text{ s}^{-1}$ and 80 ns), in addition to TCAD #1 (triangles, mobility $60 \text{ cm}^2 \text{ V}^{-1} \text{ s}^{-1}$ and defect lifetime 300 ns). Alone, the FWHM(t) evolution is not sufficient to fully determine carrier mobility because of the interplay between μ and τ_{defect} . As will be explained in the next section, it is possible to separate the respective contributions of μ and τ_{defect} using TRPL mapping data and numerical simulations to constrain the values of each parameter.

2.3. Self-Consistent data analysis and carrier mobility determination

As discussed earlier, a more detailed analysis of the TRPL mapping data is required to disentangle the effects of mobility and recombination at defects. The following strategy is adopted: first, we explore the parameter space by numerical simulations, and then we analyze both experimental and simulation data extracting indicators for the analysis to finally identify the range of parameter values leading to a reasonable match between simulations and experiments.

Figure 3 shows a flow diagram of the workflow for simulations and data analysis. We generate simulation datasets based on the model described in Section 2.2. We restrict the numerical problem to a 2D domain, as the diffusion along the vertical direction is comparatively fast (few ns) and irrelevant to our analysis.

We model a circular defective region of a given diameter d and a uniform initial carrier population. The value of d is set to the value measured experimentally at early times in FWHM(t) data (see values given in Section 5). When required, we also slightly modify the doping concentration at the defect region (details and methodology described later). The value of τ_{top} (defect-free area) is fixed to the one obtained from the fit to the experimental decay far from the defect. The input parameters are μ and τ_{defect} . The value of τ_{defect} is of low interest in itself, but its analysis is required to constrain the value of mobility. Although τ_{defect} can be approached by the local decay at early times, its value is not precisely known as the recombination at the defect is balanced by carrier drift diffusion^[33] (see Figure S1, Supporting Information).

After meshing, the software solves the drift-diffusion equation, and for each parameter set (μ , τ_{defect}) exports a carrier population $PL(t, \vec{r})$ as a function of position \vec{r} and time. We extract data on an array of $M \times M$ regions (or pixels) with region size $< 1 \mu\text{m}$. Each region contains data integrated over several meshing points and is significantly smaller than the carrier diffusion length to provide sufficient spatial resolution. Therefore, the structure and content of the data generated by one simulation run closely match the information contained in an experimental mapping data set. Therefore, in the following, we process the experimental and numerical data in a very similar manner.

The data of a simulation run (μ , τ_{defect}) are processed to extract the following four analysis curves.

1) FWHM(t): for each of the time steps, we angularly average cutlines of the $PL(t, \vec{r})$ maps into $PL(t, r)$ curves using the defect as the center of rotation. The FWHM (from a Gaussian fit) of the PL dip is reported as a function of time. In the absence of charge separation or strong electric field generated by the defect,^[19] FWHM($t = 0$) retrieves an apparent width of the defect. Therefore, we set the defect diameter to the experimental FWHM at early times.

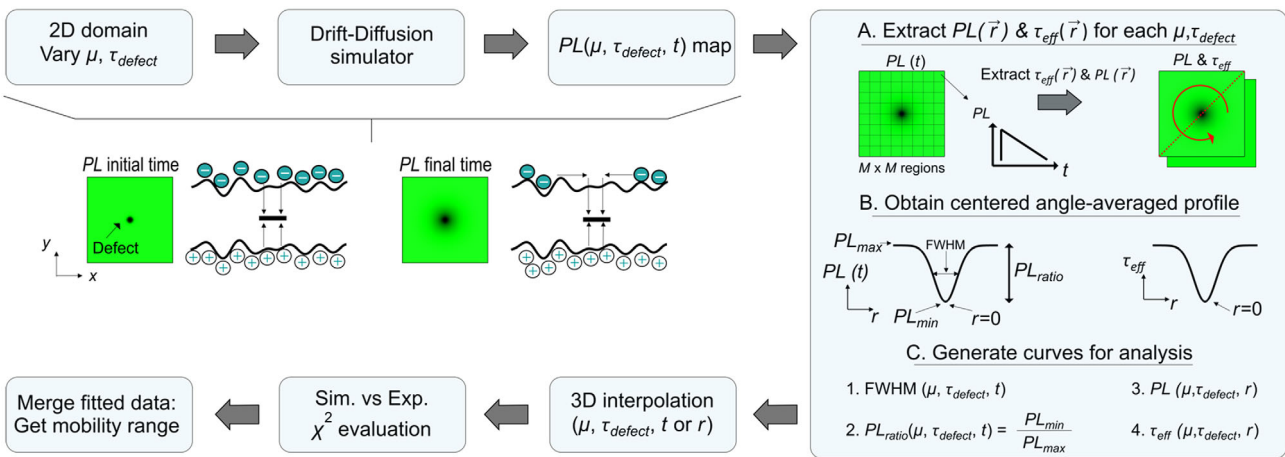


Figure 3. Simulation flow of the methodology used to analyze carrier diffusion and ultimately estimate the carrier mobility. In the middle left part, a sketch of the transport processes at initial and final times is depicted (PL maps and fluctuating bands with a trap energy level, or defect, in the middle), illustrating that at final times carriers from longer distances can recombine at the defect.

2) $PL_{ratio}(t) = \frac{PL_{min}(t)}{PL_{max}(t)}$: at any given time, we report the ratio between the minimum dip value (PL at the defect) to the average value far from the defect. In principle, $PL_{ratio} = 1$ at $t = 0$. However, this is not always the case with the experimental data (e.g., for NaF, NaF + RbF SLG (LT), and steel samples). This behavior originates from different radiative properties at the defect, i.e., independent of μ and τ_{defect} . As mentioned earlier, we modified the doping level in the defect region to match the experimental and simulated levels at early times (radiative recombination is effectively modified by the doping level).

3) $PL(r) = \int_{t_1}^t PL(t, \vec{r}) dt$ profile: angularly averaged time-integrated PL intensity as a function of the distance to the defect. $t_1 = 10$ ns to ensure vertical distribution of charge carriers—populating the notch—and t_2 is chosen as the time at which the signal drops to $1/e$ of the signal at $t = t_1$.

4) $\tau_{eff}(r)$ profile: in every simulated region (experimental pixel), the charge carrier decay is fitted using a single exponential to obtain $\tau_{eff}(\vec{r})$ which is then angularly averaged into $\tau_{eff}(r)$. Identical time windows were chosen to fit the simulations and experimental data, as for the $PL(r)$ data.

To retain a good signal-to-noise ratio, the time traces $FWHM(t)$ and $PL_{ratio}(t)$ are obtained by integrating the signal over small time intervals represented as horizontal error bars in **Figure 4a** and **Figure 4b**. Note that steel sample is treated with a line defect (1D) and centered angle-averaged profiles are not required (see Section 5). Locally, the experimental defect extends sufficiently in the vertical direction; thus, a 1D approximation is reasonable.

As shown later, some of the extracted information is highly correlated, i.e., $PL_{ratio}(t)$, $PL(r)$, and $\tau_{eff}(r)$, but the combination with the FWHM data will strongly constrain the possible values of μ . The next step is to identify the values of (μ, τ_{defect}) for which simulations have a good match with experimental datasets, as assessed by comparing the four analysis curves described earlier. To limit the required computation power, we sweep the mobility and defect lifetime over a limited number of values, and we increase the effective resolution in the (μ, τ_{defect}) parameter space by interpolation of the four sets of analysis curves. Then, for each

interpolated individual curve, $FWHM(t)$, $PL_{ratio}(t)$, $PL(r)$, and $\tau_{eff}(r)$, we evaluate the χ^2 goodness of fit to the corresponding curves extracted from experimental data. We define a threshold for a good fit χ^2 within two times its minimum achieved value, which is deviated from perfect fit, especially for $PL(r)$ and $\tau_{eff}(r)$ due to signal fluctuations. The minimum χ^2 achieved retrieves maximum deviations (at a given data point) $< 5\%$ (absolute) and in some cases up to 10% (e.g., $PL_{ratio}(t)$ for NaF + RbF at LT). These deviations are reasonable considering measurement uncertainty.

We obtain a good match for the four analysis curves simultaneously, especially in the case of NaF + RbF SLG (HT) sample, as it will be shown later. A lesser agreement is found for the other samples NaF, NaF + RbF SLG (LT), and steel: a given set of μ and τ_{defect} is not enough to explain all curves. The experimental PL at the defect is lower than the one predicted by the fitted value of τ_{eff} . The $PL_{ratio} < 1$ at early times (< 20 ns), being ≈ 0.8 for NaF and NaF + RbF SLG (LT) and 0.6 for steel. Assuming low injection conditions, $PL_{ratio} < 1$ at early times can be explained by charged impurities,^[36] doping fluctuations,^[18,36,37] or even charge carrier separation at the defect (see an example for CdTe in the study by Rau et al.^[38]). We find a change in doping concentration by 20–40% can explain the PL_{ratio} at initial time. Such values are reasonable, and resolve the discrepancy between the spatial PL and τ_{eff} data (see **Figure S2**, **S3**, Supporting Information). We note that a similar behavior can be obtained by considering a positive charge at the defect site (with band bending lower than 10 meV), with no significant changes in the final results.

Figure 4 shows the set of curves for analysis of measured (symbols) and simulated data (continuous lines), after adjustment of the doping level in the defect region (for NaF LT, NaF + RbF LT, and steel). The simulations yield a wide variety of analysis curves, but only the curves are shown for which the parameters retrieved reasonably good fits for all four analysis curves (corresponding to the gold shaded areas in **Figure 5**). For all samples, we observe a very good agreement between simulations and experiments. Specifically, the charge transport is

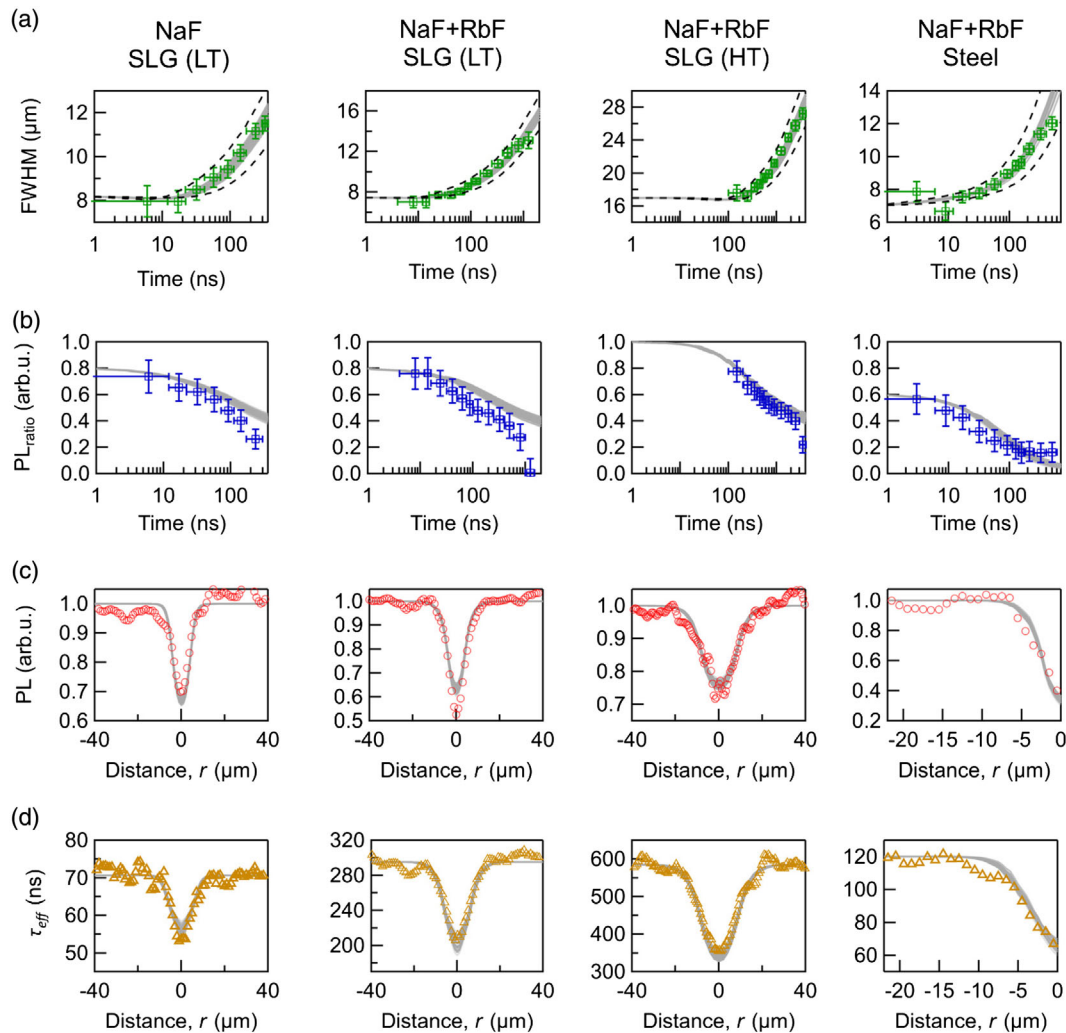


Figure 4. a) FWHM and b) PL_{ratio} as a function of time, and c) PL and d) τ_{eff} as a function of distance of the defect r for the four samples analyzed in this work. Experimental curves are shown with symbols and simulation data with solid lines. Only simulated curves are shown that result in good agreement with data of Figure 5 (gold region). In rows (a) and (b), the horizontal error bars denote the time interval for integration of experimental data, whereas vertical bars indicate fitting uncertainty to a Gaussian formula. In row (a), the dashed lines assume mobilities outside the upper and lower thresholds for accepted values ($\pm 30\%$) to illustrate the sensitivity of FWHM(t) to mobility.

limited to distances from 4 to 10 μm (FWHM in Figure 4 row a). The transient behavior of PL_{ratio} (row b) shows an initial fast drop as a result of the faster recombination rate at the defect, which saturates at late times as the carrier-depleted defect region receives a net flux of carriers from nearby regions. The defect locally reduces the time-integrated PL signal (row c) to about 30–60% of the defect-free area signal, whereas τ_{eff} (row d) confirms such PL reduction is indeed correlated with a shorter lifetime at the defect.

Finally, we identify the regions in the parameter space (μ , τ_{defect}) that results in good fits for each analysis curve, as graphically shown in Figure 5. Shaded regions display the parameter space with accepted χ^2 goodness of each analysis curve, whereas the gold regions correspond to the parameter space in which all four analysis curves yield good fits simultaneously.

As stated earlier, the criteria $PL_{\text{ratio}}(t)$, $PL(r)$, and $\tau_{\text{eff}}(r)$ are highly correlated as evidenced by the similarity of their

corresponding shaded regions. The corresponding shaded regions present a reasonable overlap and mostly constrain the defect properties (τ_{defect}). In contrast, the shaded regions of the FWHM(t) criterion are almost vertical and restrict the possible values for mobility; however, relatively weaker combination of the four criteria provides a narrow range for the possible mobility values. Consistently, the defect lifetime is highly constrained and its value is lower than the experimental decay time, as expected. **Table 1** shows the transport properties estimated in this work.

3. Discussion

We have shown a good agreement between modeling and experimental datasets of transport and recombination of charge carriers near extended defects. Despite the good agreement, our modeling made assumptions that might affect the analysis.

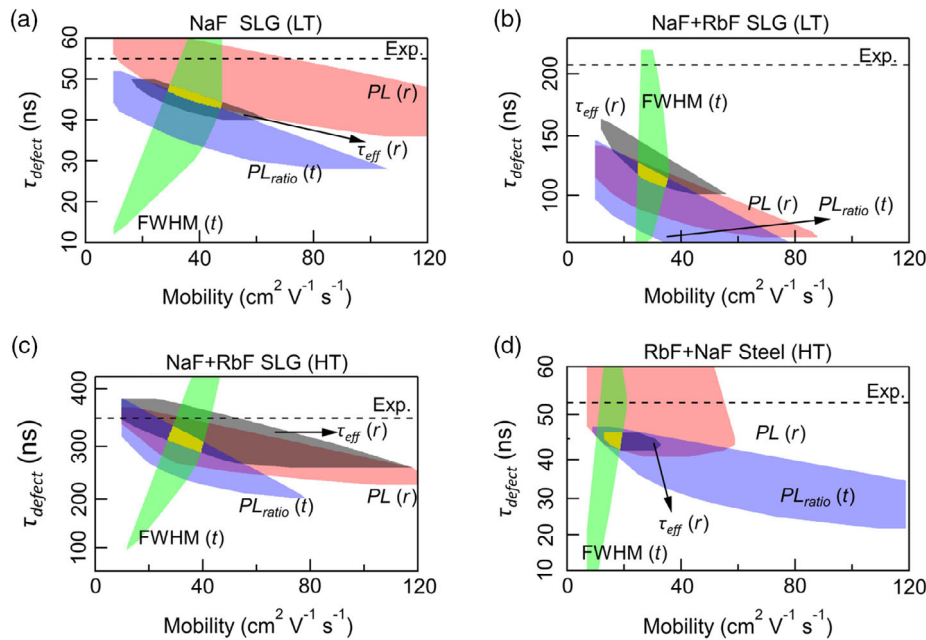


Figure 5. Representation of the parameter space (τ_{defect} and mobility) for all samples analyzed. The shaded regions correspond to accepted fits to the experimental datasets. The gold region corresponds to the intersection of the four shaded regions, for which the individual curves as shown as solid lines in Figure 4. The horizontal dashed lines correspond to the experimental lifetime value.

Table 1. Carrier mobility, effective carrier lifetime τ (evaluated in the full time window), and diffusion length for the four samples analyzed in this work.

Sample substrate	PDT	μ [cm ² V ⁻¹ s ⁻¹]	τ [ns]	L_D [μ m]
SLG (LT)	NaF	26 to 50	105	2.7–3.7
SLG (LT)	NaF + RbF	23 to 37	570	5.8–7.4
SLG (HT)	NaF + RbF	25 to 42	780	7.1–9.2
Steel (HT)	NaF + RbF	9 to 21	155	1.9–2.9

In the following, we discuss the possible influence of electric drift in our analysis. Then, we compare the results to previous literature, suggest limiting mechanisms for mobility, and highlight the implications of the transport properties on device performance.

Electric drift transport arises from local electric fields (or band bending) induced by grain boundaries (GBs), material inhomogeneities, or the presence of an extended defect as in our study (e.g., dislocations, strain, etc.). The electrical activity at the defect can be modified by charge separation, charged impurities, among other mechanisms. Because our modeling did not include such local band bending and charging, we evaluate their implications considering a worst-case scenario. Following the reasoning of Gfroerer et al.,^[31] let us assume a defect (or GB, or material inhomogeneity) that induces Fermi-level pinning at the middle of the bandgap. The depletion width (W) near the defects follows $W = \sqrt{2\epsilon_s V_b / qN_A}$,^[39] where ϵ_s is the absolute dielectric constant of the semiconductor, V_b the built-in voltage, and N_A the doping density. For $V_b = E_g/2$ (half of

the bandgap) and N_A ranging between $3 \times 10^{15} \text{ cm}^{-3}$ to $3 \times 10^{16} \text{ cm}^{-3}$, W is approximately 150 nm for steel and 500 nm for the other samples. These values correspond to the distance over which drift can be the driving force for carrier transport. Our estimates for the diffusion lengths between 2 μ m (steel) and 9 μ m are at least 10 times larger than the possible depletion width, indicating electric drift should not dominate the transport to the defect. The Fermi-level pinning at $E_g/2$ is an extreme scenario, as the defects investigated exhibit a mere 40–70% reduction in PL intensity as compared with the defect-free area. Moreover, carriers would take less than 10 ns to travel such distances. Therefore, drift near the defect would only dominate at short-range scales. Indeed, Kuciauskas et al. detected drift transport at short time scales when analyzing CdTe double heterostructures.^[19] It was found that FWHM of a Gaussian fit to PL along an extended defect doubles its value at initial times (from FWHM ≈ 5 to 10 μ m within 3 ns). This rapid increase was attributed to the presence of a strong electric field near the extended defect, as measured by second-harmonic-generation microscopy. In that specific case, the band bending was estimated between 200 and 400 meV. In our work, the experimental lifetimes at the defect remain comparable with that in the defect-free region (approximately less than threefold reduction), whereas Kuciauskas et al. characterized considerably more detrimental defects with several orders of magnitude lifetime reduction. Overall, the good agreement between the modeling and experiments, and the relatively weak detrimental influence of the defect indicate diffusion is the dominant transport mechanism in the investigated timescales.

According to our analysis, the estimated mobility lies in the range of 10–50 cm² V⁻¹ s⁻¹ for all samples studied. Our values are clearly lower than THz-spectroscopy values reported for

stoichiometric CuInSe_2 ($1000 \text{ cm}^2 \text{ V}^{-1} \text{ s}^{-1}$) and Cu-poor CuInSe_2 ($200 \text{ cm}^2 \text{ V}^{-1} \text{ s}^{-1}$)^[26] layers. A discrepancy is not surprising because THz spectroscopy measures intragrain mobility, whereas we probe the long-distance lateral transport that is affected by additional carrier scattering mechanisms. GB scattering is one of them. It is known that high growth temperatures result in larger grain sizes.^[40] If GB scattering were limiting the mobility, we would expect higher mobility for samples grown at high temperatures. Interestingly, the comparison of the SLG samples reveals no clear impact of substrate temperature and RbF-PDT on mobility. This suggests that carrier transport is not affected by the higher number of GBs, and is instead limited by other scattering mechanisms within the grains. Our samples are near-stoichiometric, with CGI values ranging 0.93–0.95 and with GGI values ranging 0.32–0.4 (see Table S1, Supporting Information). Absorber compositions with higher Ga-content may result in higher densities of point defects in the grain interiors,^[41,42] and result in lower mobilities due to the expected alloy or impurity scattering as compared with those found in previous studies.^[4,26] This is not necessarily the case for steel sample, which has the lowest bandgap—thus Ga content—(see Table S1, Supporting Information), and the lowest mobility of all samples studied. We estimate for sample steel a mobility range of about half of the values of the SLG samples. This can be attributed to its higher doping concentration revealed by $C-V$ (see Figure S4, Supporting Information) and suggests that impurity scattering might be limiting the mobility in highly doped CIGS layers. The mobility estimates found in this work are in good agreement with recent results from ultrafast transient spectroscopy in samples very similar to the ones investigated here.^[30]

Finally, we highlight the implications of the transport properties on device performance, and specifically, on the charge carrier collection, open-circuit voltage, and fill factor (FF). The diffusion lengths found (≈ 2 to $9 \mu\text{m}$) are not a limiting factor for charge carrier collection for state-of-the-art CIGS absorbers with optically active film thicknesses $< 1.5 \mu\text{m}$. This is valid even in the hypothetical absence of the space charge region. For thicker absorbers ($> 2 \mu\text{m}$) such as those suited to tandem solar cell designs—and without back reflector—only sample steel could impose a limit to carrier collection. No impact of L_D on back surface recombination is expected because nearly complete passivation is typically accomplished by the back grading of state-of-the-art CIGS solar cells.^[43] On the contrary, for ultrathin CIGS absorbers (hundreds of nm) with partial (or null) back contact passivation, enhanced mobility negatively affects device V_{OC} . Similar implications could be expected for next-generation CIGS solar cells implementing selective contacts with partial or complete back contact passivation. Concerning majority carrier transport, the mobilities and corresponding doping concentrations provide sufficient layer conductivity without compromising the FF in current device architecture.

4. Conclusions

We have investigated the diffusion and recombination of charge carriers near extended defects and derived their mobility in high-quality CIGS absorbers under low injection conditions.

We compared different experimental setup configurations to extract mobility of charge carriers based on TRPL mapping: profiles differ for recombination at defect after uniform excitation or for diffusion after localized injection. We have shown how to decouple the effects of recombination and charge transport by combining experimental data and numerical simulations.

We acquired TRPL mapping datasets with uniform wide-field illumination and low-injection condition on CIGS absorbers fabricated at different deposition temperatures on different substrates and subjected to different alkali treatments. The data acquisitions were centered on extended defective regions. Due to carrier diffusion, the dip in the PL signal expands over time after the initial excitation. We performed numerical simulations of carrier diffusion transport and recombination, modeling the defects as regions with increased recombination rates. Comparison of extracted analysis curves effectively constrained the possible values of carrier mobility within a narrow interval.

We report carrier mobility in the same order of magnitude for all samples analyzed, in the range $10\text{--}50 \text{ cm}^2 \text{ V}^{-1} \text{ s}^{-1}$. Rb heavy alkali incorporated by PDT does not affect the carrier mobility. As compared with processes compatible with polyimide substrates, high growth temperatures result in larger grain sizes. However, we found no change in carrier mobility with deposition temperature, suggesting that carrier mobility is not limited by grain boundaries, but instead by other scattering mechanisms related to the grain interior. The comparatively lower mobility values observed for the sample on steel with higher doping concentration suggest that impurity scattering may become a limiting factor to mobility in highly doped CIGS layers.

5. Experimental Section

Samples Description: Double graded CIGS absorbers of about $3 \mu\text{m}$ total thickness were grown on different substrates, namely, SLG and stainless-steel (here referred to as steel). Two different postdeposition treatments were applied: NaF and NaF + RbF with a finishing cap of RbF at the end of the third stage. LT growth corresponds to actual $\approx 450^\circ\text{C}$, and HT to about 580°C . Sample steel was grown at HT with PDT process NaF + RbF. The solar cells were completed with chemical bath deposition of CdS and sputtered ZnO/AlZnO layers. The solar cells exhibit different performance levels, i.e., approximately 17–20% efficiency (≈ 370 to $460 \text{ mV } V_{OC}$ deficit). Table S1, Supporting Information shows the PV parameters. More details on the growth, alkali PDT process, and device fabrication can be found elsewhere.^[44] For TRPL measurements, the transparent conductive oxide has been etched away for 5 min in a 5% acetic acid solution to prevent carrier extraction by the front electrode. Therefore, the sample structure for TRPL is CdS/CIGS/Mo. The influence of CdS on the transients is negligible in our samples, in agreement with Metzger et al.^[22] and Weiss et al.^[24]

TRPL Mapping: A MicroTime 100 system coupled to a detection unit from PicoQuant was used for TRPL mapping. For excitation, a laser of 639 nm with $< 100 \text{ ps}$ pulse duration was used with frequencies between 100 kHz and 1 MHz . The beam size was about $130 \mu\text{m}$ (" 13.5% metric"), as measured by a NanoScan2 beam profiler. A long-range $20\times$ objective optimized for the NIR transmission (Olympus LCPLN20XIR) was used with a numerical aperture of 0.45. For detection, an optical fiber of $50 \mu\text{m}$ diameter acting as a pinhole collects the light coming from the objective to the entrance of a FluoTime 300 unit from PicoQuant. The FluoTime 300 includes collection optics to guide the light into the monochromator, which is coupled to an InGaAs-based photomultiplier (PMT) detector from Hamamatsu (H10330A-45). For photon counting,

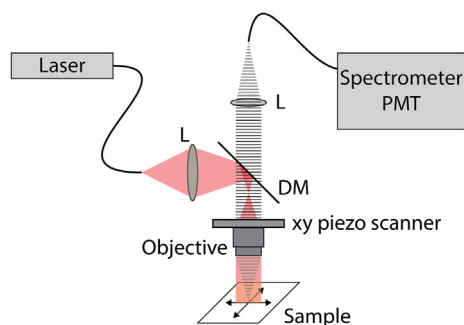


Figure 6. General illustration of the TRPL mapping setup. L, Lens; DM, dichroic mirror; PMT, photomultiplier.

PicoQuant TCSPC cards in the long-range mode were used to avoid pile-up effects. Using the $20\times$ objective and a tube lens, the samples are imaged with $20\times$ magnification onto the collection fiber ($50\ \mu\text{m}$ diameter). The collection spot size is therefore about $2.5\ \mu\text{m}$. By setup construction, the collection spot ($\approx 2.5\ \mu\text{m}$) is always located at the center of the much larger illumination spot ($\approx 130\ \mu\text{m}$). The objective is coupled into a fine piezo scanner with nm-spatial resolution from Physik instrumente (PI P-733.2). Therefore, time-resolved PL data (spectrally integrated) were spatially resolved and recorded in a pixel-by-pixel basis. Maps of $80\times 80\ \mu\text{m}^2$ were acquired with pixel size of $0.625\times 0.625\ \mu\text{m}^2$ and $1\times 1\ \mu\text{m}^2$. Acquisition times range 150–250 ms per pixel. **Figure 6** shows a simplified illustration of the TRPL mapping setup.

To achieve low injection conditions, the system was used in a uniform illumination/local detection configuration. Uniform (or wide-field) illumination was set by focusing the beam to the back focal plane of the objective, and a collimated beam was projected onto the sample. A photon density of $\approx 3\times 10^{11}\ \text{cm}^{-2}\ \text{pulse}^{-1}$ was used. The initial injection was $8\times 10^{15}\ \text{cm}^{-3}$ assuming $\alpha = 6\times 10^4\ \text{cm}^{-1}$.^[1] After few nanoseconds ($<10\ \text{ns}$), the carriers redistribute vertically in the absorber region of $1.5\ \mu\text{m}$ with a low bandgap; thus, the carrier density reduces to about $2\times 10^{15}\ \text{cm}^{-3}$. The apparent doping concentration was approximated from capacitance–voltage measurements ranging $3\times 10^{15}\ \text{cm}^{-3}$ to $3\times 10^{16}\ \text{cm}^{-3}$ (see Figure S4, Supporting Information). Therefore, the minimum photon density used is expected to correspond to low injection conditions. A detailed analysis of power-dependent TRPL mapping and estimation of injection conditions on these samples will be published elsewhere.^[25]

Examples of experimental data are shown in Figure S1, Supporting Information. The time window chosen to fit the decays was taken from the time when carriers are distributed through the absorber (about 10 ns after the initial peak) to the time for which the PL reached $1/e$ of the first fitted point. In this range, a single exponential equation was sufficient to perform reasonable fits. Our TRPL decays are not single exponential (see Figure S1, Supporting Information); however, as discussed earlier, we choose a short time window with well-behaved decays to analyze carrier diffusion.

Drift-Diffusion Simulations: Simulations have been conducted in Sentaurus modeling framework from Synopsys.^[45] A 2D domain is considered with an area up to $200\times 200\ \mu\text{m}$ depending on the sample. Because we are under wide-field illumination and carriers diffuse to the notch faster than 10 ns, the third dimension corresponding to the depth of the structure is not considered. Zero current is set to the contacts to emulate open-circuit conditions. A pulsed generation rate corresponding to low injection conditions was set. Surface recombination is neglected. Carriers are relatively inhibited to recombine at surfaces due to the front grading (and CdS presence),^[24] and especially the back bandgap grading.^[46] The absorber properties are uniform, disregarding the defect region, which is modeled by a circular central region with different carrier lifetimes. The diameter of the defect is fixed, being 4, 3.5, and $8.5\ \mu\text{m}$ for NaF, NaF + RbF (LT), and NaF + RbF (HT), respectively.

These values are chosen according to the procedure described in the main manuscript. As for the steel sample, the simulation domain is a 1D line of $200\ \mu\text{m}$ and a central defect of $3.5\ \mu\text{m}$. Further details about the modeling and material parameters can be found elsewhere.^[47]

Supporting Information

Supporting Information is available from the Wiley Online Library or from the author.

Acknowledgements

This work received financial support partially from the Swiss State Secretary for Education, Research and Innovation (SERI) under contract number 17.00105 (EMPIR project HyMet) and from the Swiss Federal Office of Energy (SFOE) (SI/501614-01 “ImproCIS”). The EMPIR program was cofinanced by the Participating States and by the European Union’s Horizon 2020 research and innovation program.

Open access funding provided by Lib4RI Library for the Research Institutes within the ETH Domain Eawag Empa PSI and WSL.

[Correction added on April 7, 2022, after first online publication: CSAL funding statement has been added.]

Conflict of Interest

The authors declare no conflict of interest.

Data Availability Statement

The data that support the findings of this study are available from the corresponding author upon reasonable request.

Keywords

carrier mobility, charge carrier transport, CIGS, simulation, time-resolved photoluminescence mapping

Received: June 9, 2021
Revised: July 5, 2021
Published online: August 6, 2021

- [1] R. Carron, E. Avancini, T. Feurer, B. Bissig, P. A. Losio, R. Figi, C. Schreiner, M. Bürki, E. Bourgeois, Z. Remes, M. Nesladek, S. Buecheler, A. N. Tiwari, *Sci. Technol. Adv. Mater.* **2018**, *19*, 396.
- [2] W. Metzger, R. Ahrenkiel, P. Dippo, *Department of Energy Solar Energy Technologies Program Rev. Meeting* **2004**, *1*, pp. 1–2.
- [3] D. Kuciauskas, D. Krasikov, *IEEE J. Photovoltaics* **2018**, *8*, 1754.
- [4] T. Unold, H. Hempel, C. Strothkamper, C. A. Kaufmann, R. Eichberger, A. Bartelt, *2014 IEEE 40th Photovoltaic Specialist Conf.*, IEEE, Piscataway, NJ, USA **2014**, pp. 2066–2069.
- [5] D. J. Wolford, G. D. Gilliland, T. F. Kuech, J. A. Bradley, H. P. Hjalmarson, *Phys. Rev. B* **1993**, *47*, 15601.
- [6] N. M. Haegel, T. J. Mills, M. Talmadge, C. Scandrett, C. L. Frenzen, H. Yoon, C. M. Fetzer, R. R. King, *J. Appl. Phys.* **2009**, *105*, 023711.
- [7] P. Würfel, T. Trupke, T. Puzzer, E. Schäffer, W. Warta, S. W. Glunz, *J. Appl. Phys.* **2007**, *101*, 123110.
- [8] C. Donolato, *Appl. Phys. Lett.* **1985**, *46*, 270.
- [9] F. Frühauf, O. Breitenstein, *Sol. Energy Mater. Sol. Cells* **2018**, *174*, 277.

- [10] J. Moseley, P. Rale, S. Collin, E. Colegrove, H. Guthrey, D. Kuciauskas, H. Moutinho, M. Al-Jassim, W. K. Metzger, *J. Appl. Phys.* **2018**, *124*, 113104.
- [11] T. Kirchartz, U. Rau, M. Kurth, J. Mattheis, J.H. Werner, *Thin Solid Films* **2007**, *515*, 6238.
- [12] T. Unold, L. Gütay, *Advanced Characterization Techniques for Thin Film Solar Cells Second Edition*, Vol. 1–2, Wiley-VCH, Weinheim, Germany **2016**, pp. 275–297.
- [13] A. Bercegol, G. El-Hajje, D. Ory, L. Lombez, *J. Appl. Phys.* **2017**, *122*, 203102.
- [14] H. Hempel, C. J. Hages, R. Eichberger, I. Repins, T. Unold, *Sci. Rep.* **2018**, *8*, 14476.
- [15] S. A. Dinca, E. A. Schiff, W. N. Shafarman, B. Egaas, R. Noufi, D. L. Young, *Appl. Phys. Lett.* **2012**, *100*, 103901.
- [16] S. Johnston, T. Unold, I. Repins, R. Sundaramoorthy, K. M. Jones, B. To, N. Call, R. Ahrenkiel, *J. Vac. Sci. Technol. A Vac. Surf. Film* **2010**, *28*, 665.
- [17] B. Bissig, C. Guerra-Nunez, R. Carron, S. Nishiwaki, F. La Mattina, F. Pianezzi, P. A. Losio, E. Avancini, P. Reinhard, S. G. Haass, M. Lingg, T. Feurer, I. Utke, S. Buecheler, A. N. Tiwari, *Small* **2016**, *12*, 5339.
- [18] M. Kawamura, T. Yamada, N. Suyama, A. Yamada, M. Konagai, *Jpn. J. Appl. Phys.* **2010**, *49*, 0623011.
- [19] D. Kuciauskas, T. H. Myers, T. M. Barnes, S. A. Jensen, A. M. Allende Motz, *Appl. Phys. Lett.* **2017**, *110*, 083905.
- [20] N. M. Haegel, S. E. Williams, C. Frenzen, C. Scandrett, *Phys. B Condens. Matter* **2009**, *404*, 4963.
- [21] M. Maiberg, T. Hölscher, S. Zahedi-Azad, W. Fränzel, R. Scheer, *Appl. Phys. Lett.* **2015**, *107*, 122104.
- [22] W. K. Metzger, I. L. Repins, M. A. Contreras, *Appl. Phys. Lett.* **2008**, *93*, 022110.
- [23] S. A. Jensen, S. Glynn, A. Kanevce, P. Dippo, J. V. Li, D. H. Levi, D. Kuciauskas, *J. Appl. Phys.* **2016**, *120*, 063106.
- [24] T. P. Weiss, R. Carron, M. H. Wolter, J. Löckinger, E. Avancini, S. Siebentritt, S. Buecheler, A. N. Tiwari, *Sci. Technol. Adv. Mater.* **2019**, *20*, 313.
- [25] M. Ochoa, S. Yang, S. Nishiwaki, A. N. Tiwari, R. Carron, unpublished.
- [26] C. Strothkämper, A. Bartelt, R. Eichberger, C. Kaufmann, T. Unold, *Phys. Rev. B* **2014**, *89*, 115204.
- [27] D. Kuciauskas, J. V. Li, A. Kanevce, H. Guthrey, M. Contreras, J. Pankow, P. Dippo, K. Ramanathan, *J. Appl. Phys.* **2015**, *117*, 185102.
- [28] D. Kuciauskas, J. V. Li, M. A. Contreras, J. Pankow, P. Dippo, M. Young, L. M. Mansfield, R. Noufi, D. Levi, *J. Appl. Phys.* **2013**, *114*, 154505.
- [29] T. P. Weiss, B. Bissig, T. Feurer, R. Carron, S. Buecheler, A. N. Tiwari, *Sci. Rep.* **2019**, *9*, 5385.
- [30] Y.-H. Chang, R. Carron, M. Ochoa, C. Bozal-Ginesta, A. N. Tiwari, J. R. Durrant, L. Steier, *Adv. Energy Mater.* **2021**, *11*, 2003446.
- [31] T. H. Gfroerer, Y. Zhang, M. W. Wanlass, *Appl. Phys. Lett.* **2013**, *102*, 012114.
- [32] F. Chen, Y. Zhang, T. H. Gfroerer, A. N. Finger, M. W. Wanlass, *Sci. Rep.* **2015**, *5*, 10542.
- [33] B. Fluegel, K. Alberi, M. J. DiNezza, S. Liu, Y.-H. Zhang, A. Mascarenhas, *Phys. Rev. Appl.* **2014**, *2*, 034010.
- [34] S. M. Sze, K. K. Ng, *Physics Of Semiconductor Devices*, John Wiley & Sons, Inc., Hoboken, NJ, USA **2006**.
- [35] M. Krause, A. Nikolaeva, M. Maiberg, P. Jackson, D. Hariskos, W. Witte, J. A. Márquez, S. Levchenko, T. Unold, R. Scheer, D. Abou-Ras, *Nat. Commun.* **2020**, *11*, 4189.
- [36] D. Abou-Ras, N. Schäfer, C. J. Hages, S. Levchenko, J. Márquez, T. Unold, *Sol. RRL* **2018**, *2*, 1700199.
- [37] A. Nikolaeva, M. Krause, J. Marquez, C. Hages, S. Levchenko, T. Unold, W. Witte, D. Hariskos, D. Abou-Ras, *2018 IEEE 7th World Conf. on Photovoltaic Energy Conversion (WCPEC) (A Joint Conf. of 45th IEEE PVSC, 28th PVSEC & 34th EU PVSEC)*, IEEE, Piscataway, NJ, USA **2018**, pp. 2512–2514.
- [38] C. Li, Y. Wu, T. J. Pennycook, A. R. Lupini, D. N. Leonard, W. Yin, N. Paudel, M. Al-Jassim, Y. Yan, S. J. Pennycook, *Phys. Rev. Lett.* **2013**, *111*, 1.
- [39] U. Rau, K. Taretto, S. Siebentritt, *Appl. Phys. A* **2009**, *96*, 221.
- [40] P. M. P. Salomé, A. Hultqvist, V. Fjällström, B. Vermang, M. Edoff, B. Aitken, K. Zhang, K. Fuller, C. K. Williams, *Sol. Energy Mater. Sol. Cells* **2014**, *123*, 166.
- [41] J. T. Heath, J. D. Cohen, W. N. Shafarman, D. X. Liao, A. A. Rockett, *Appl. Phys. Lett.* **2002**, *80*, 4540.
- [42] C. Persson, A. Zunger, *Appl. Phys. Lett.* **2005**, *87*, 211904.
- [43] S.-C. Yang, M. Ochoa, R. Hertwig, A. Aribia, A. N. Tiwari, R. Carron, *Prog. Photovoltaics* **2021**, *29*, 630.
- [44] R. Carron, S. Nishiwaki, T. Feurer, R. Hertwig, E. Avancini, J. Löckinger, S.-C. Yang, S. Buecheler, A. N. Tiwari, *Adv. Energy Mater.* **2019**, *9*, 1900408.
- [45] Synopsys, *Sentaurus Device User Guide. Version P-2019.3*, **2019**.
- [46] T. Feurer, B. Bissig, T. P. Weiss, R. Carron, E. Avancini, J. Löckinger, S. Buecheler, A. N. Tiwari, *Sci. Technol. Adv. Mater.* **2018**, *19*, 263.
- [47] M. Ochoa, S. Buecheler, A. N. Tiwari, R. Carron, *Energy Environ. Sci.* **2020**, *13*, 2047.